Vortex-glass transition, pinning mechanisms, and vortex dynamics in NbRe films and NbRe/Py bilayers

Abhishek Kumar,[1,2,*] F. Avitabile,[1] F. De Chiara,[1] F. Colangelo,[1,2] Z. Makhdoumi Kakhaki,[1,†] C. Cirillo,[2] and C. Attanasio[1,2,3]

[1]*Dipartimento di Fisica "E. R. Caianiello", Università degli Studi di Salerno, I-84084 Fisciano (SA), Italy*

[2]*CNR-SPIN, c/o Università degli Studi di Salerno, I-84084 Fisciano (SA), Italy*

[3]*Centro NANO_MATES, Università degli Studi di Salerno, I-84084 Fisciano (SA), Italy*

(Received 20 February 2026; revised 6 August 2026; accepted 21 September 2026; published 4 November 2026)

We present a comparative study of vortex-glass (VG) phase, vortex pinning, and vortex dynamics in superconducting niobium-rhenium (NbRe) films and NbRe/permalloy bilayers fabricated by the dc magnetron sputtering technique, where permalloy (Py) serves as the ferromagnetic layer. Current-voltage characteristics were measured as a function of temperature and magnetic field to investigate the VG transition, analyzed through scaling laws to determine the VG phase line, $H_g(T)$. NbRe films exhibit systematically higher $H_g(T)$ magnitude than the NbRe/Py bilayers, indicating stronger vortex pinning in the former. The reduced $H_g(T)$ trend observed in the NbRe/Py bilayers is attributed to the superconducting proximity effect and the homogeneous magnetic exchange interaction at the NbRe/Py interface. To further elucidate the pinning properties, critical current densities and pinning forces were evaluated, revealing that vortex pinning is strongly influenced by structural inhomogeneities and disorder in both systems, with consistently larger pinning forces in NbRe films. The weaker pinning in NbRe/Py bilayers is reflected in their vortex-instability behavior, characterized significantly by their higher vortex velocities compared to NbRe films.

DOI: 10.1103/jgmf-dgxg

I. INTRODUCTION

The mixed state of type-II superconductors has long attracted considerable attention due to the rich variety of magnetic phases it exhibits, which provide insight into fundamental superconductivity phenomena. Notable examples include the vortex glass (VG) transition [1–10], Bose metal phase [11,12], quantum Griffith singularity [13,14], and phase-slip phenomena [15,16]. These phases are governed by the interplay of vortex dynamics, thermal fluctuations (TFs), and superconducting or quantum fluctuations (SFs or QFs). Among them, the VG phase plays a critical role in determining vortex dynamics and, consequently, the performance of superconducting materials.

In type-II superconductors, an applied magnetic field (B) induces a mixed state where magnetic flux penetrates the material in the form of quantized vortices. In clean or well-ordered superconductors, these vortices form an Abrikosov lattice [17], whose structure and dynamics are strongly influenced by quenched disorder arising from defects, impurities, or structural inhomogeneities. Such disorder acts as pinning centers, immobilizing vortices and enabling a finite critical current density (J_c). TFs can drive a transition from a zero-resistance VG phase to a resistive vortex-liquid state. Fisher *et al.* [18] described this as a disorder-driven continuous VG transition, in which a zero-resistance VG phase transforms into a vortex liquid one with finite resistivity at critical magnetic field, H_g, and critical temperature, T_g. Near these critical parameters, the system exhibits universal scaling behavior, with correlation length $\xi \sim |T - T_g|^{-\nu}$ or $\xi \sim |H - H_g|^{-\nu}$ and relaxation time $\tau \sim \xi^z$ [1,19].

From an experimental perspective, understanding how defects pin vortices and influence their dynamics under applied currents is essential for nanoscale superconducting devices. Current-driven Lorentz forces and TFs can induce creeplike vortex motion, degrading dissipation-free transport [20]. In the VG phase, tightly pinned vortices determine the J_c, which in turn affects potential applications [21,22]. The pinning mechanisms can be analyzed through current-voltage characteristics (IVCs) measured under varying magnetic fields and temperatures. Pinning behavior may arise from spatial variations in the superconducting order parameter (δT_c pinning, where T_c is the superconducting transition temperature) or from fluctuations in the charge-carrier mean free path (δl pinning) due to structural defects and grain boundaries [19,23]. Additionally, the magnetic field dependence of J_c can be characterized by the pinning force, which reflects the strengthening or weakening of vortex immobilization by structural disorder [24].

*Contact author: abkumar@unisa.it

†Present address: Cryogenic Quantum Electronics, Institute for Electrical Measurement Science and Fundamental Electrical Engineering (EMG) and Laboratory for Emerging Nanometrology (LENA), Technische Universitt Braunschweig, 38106 Braunschweig, Germany.

Published by the American Physical Society under the terms of the Creative Commons Attribution 4.0 International license. Further distribution of this work must maintain attribution to the author(s) and the published article's title, journal citation, and DOI.

VG transition theory and pinning mechanisms remain central to understanding vortex dynamics and dissipation in both high-T_c (HTS) and low-T_c (LTS) superconductors. Experimental studies on materials such as $YBa_2Cu_3O_7$ [1], $Bi_2Sr_{2-x}La_xCuO_{6+\delta}$ [2,3], $Pr_{2-x}Ce_xCuO_{4-\gamma}$ [4], $Ba(Fe_{0.93}Co_{0.07})_2As_2$ [25], layered and homogeneous Ta/Ge films [26], Nb [5,6], NbTiN [8], TiO [10], FeSe [9], and MgB_2 [7] have explored VG behavior in both two-dimensional (2D) and three-dimensional (3D) limits. Notably, in Nb films, quasi-2D VG scaling describes IVCs of films thinner than 44 nm, whereas 3D scaling applies for thicker (100 nm) films [5,6].

The noncentrosymmetric niobium-rhenium ($Nb_{0.18}Re_{0.82}$, NbRe) superconductor [27] has not yet been explored in the context of the VG phase transition, making it the focus of the present study. Previous works on NbRe films and NbRe/ferromagnet (S/F) heterostructures [28,29] have investigated vortex instabilities through the critical vortex velocity (v^*), revealing fast quasiparticle relaxation and potential application as in superconducting single-photon detectors (SSPDs). NbRe films have also been successfully fabricated and tested in microstrip and nanomeander single-photon detectors [30–33] and further explored in spintronics and spin-valve devices when combined with ferromagnets [34,35].

In this work, we fabricated NbRe films and $NbRe/Ni_{0.80}Fe_{0.20}$ (NbRe/Py) bilayers using a dc magnetron sputtering technique. Samples of comparable dimensions were investigated to directly assess the influence of a ferromagnetic layer on vortex dynamics, including VG transition, vortex pinning, and vortex instabilities, via IVC measurements. Analysis of IVCs and J_c under varying magnetic fields and temperatures reveal a quasi-2D VG transition, enabling the construction of VG phase diagrams. The temperature dependence of J_c in different fields was interpreted considering the coexistence of δT_c and δl pinning mechanisms. Finally, vortex instabilities were systematically studied, showing higher v^* in NbRe/Py bilayers compared to NbRe films.

II. EXPERIMENTAL METHODS

The NbRe films and NbRe/Py bilayers were deposited using a dc magnetron sputtering system, employing high-purity NbRe (99.99%) and Py (99.9%) targets from Testbourne Ltd. Devices were fabricated on prepatterned silicon (Si) substrates in a Hall-bar geometry, prepared by lift-off technique via optical photolithography in a cleanroom environment. Film depositions were carried out at room temperature in an ultra-high vacuum chamber (base pressure about 2×10^{-8} mbar) under an argon (Ar) partial pressure environment of 6.5 μbar, with fixed sputtering powers of 350 W for NbRe and 150 W for Py.

For the present study, NbRe films were prepared with thicknesses of 30 nm (10 μm width) and 15 nm (20 and 10 μm widths), referred to as S1, S2, and S3, respectively. To investigate the effect of a ferromagnet on the superconducting properties, a Py layer was deposited on top of NbRe, forming NbRe/Py bilayers of comparable dimensions with thicknesses of 30/20 nm (7.6 μm width) and 15/4 nm (20 and 10 μm widths), labeled as B1, B2, and B3, respectively. The distance between the voltage terminals was kept constant at 1 mm for all samples except S2 (1.5 mm) and B1 (0.1 mm) as listed in Table I. Sample B1 was patterned into a conventional four-probe geometry using a different procedure, namely optical lithography with direct laser writer exposure, followed by ion etching, as reported elsewhere [29].

Film thicknesses were monitored using a calibrated quartz crystal microbalance and verified with a stylus profilometer (Bruker DektakXT). Electrical contacts were made via a TPT wire bonder in a conventional four-probe configuration. The resistance versus temperature, $R(T)$, and IVC measurements were performed using a current source Keithley 6221 operating together with a nanovoltmeter Keithley 2182A, assisted to a cryogen-free system (Cryogenic Ltd., 2 K, 7 T). The $R(T)$ measurements were performed in delta-mode configuration with an applied current of 10 μA. The IVCs were measured in pulse-mode configuration under perpendicular magnetic fields at different temperatures for fixed field values, and vice versa, for all NbRe films and NbRe/Py bilayers.

III. SUPERCONDUCTING TRANSITIONS

Figure 1 shows the $R(T)$ characteristics measured in the temperature range, 3–8 K, without an externally applied magnetic field for the NbRe films (main panel) and NbRe/Py bilayers (inset). The NbRe films curves are denoted by solid symbols, whereas the corresponding NbRe/Py bilayers are represented by open symbols for consistency throughout the manuscript, allowing a direct comparison of their respective behaviors. For clear representation, the resistance of sample B1 in the inset $R(T)$ plot has been multiplied by a factor of 100, since its normal state resistance is much lower than that of the other samples. The T_c values were determined from $R = R_N/2$ criterion, where R_N is the normal-state resistance at 8 K, and are listed in Table I for all NbRe films and NbRe/Py bilayers.

For NbRe films, the reduction in T_c accompanied by an increase in R_N (see Table I) is attributed to the restricted electron conduction pathways as the film thickness decreases. In NbRe/Py bilayers (B2, B3), the decrease in T_c is mainly due to the superconducting proximity effect with the ferromagnetic layer, in addition to the dimensionality effect, similar to NbRe films. In the case of B1, the lowest T_c is observed because the relatively thicker Py layer suppresses superconductivity to a greater extent, leading to a greater reduction of the superconducting order parameter in the NbRe layer.

IV. SCALING OF VORTEX-GLASS TRANSITION IN IVC

The VG transition can be analyzed by determining H_g and T_g from the IVCs, measured as a function of the magnetic field and the temperature, respectively. For $T > T_g$ and $H > H_g$, the I–V curves display an ohmic behavior at low currents, while for $T < T_g$ and $H < H_g$, they exhibit concave nonlinearity. At $T \sim T_g$ and $H \sim H_g$, the I–V curves follow a power-law dependence. To elucidate the VG characteristics, IVCs were measured for all NbRe and NbRe/Py samples under varying temperatures and magnetic fields. For the present IVC measurements, we apply external magnetic fields well above the saturation field of the Py layer (for example, the saturation

TABLE I. Sample dimensions (thicknesses, widths, lengths), superconducting transition temperature (T_c), normal state resistance (R_N), upper critical field [$H_{c2}(0)$], critical vortex glass magnetic field (H_g), and fitting parameters (D, z, and ν) in vortex-glass analysis for NbRe films and NbRe/Py bilayers.

Sample	Thickness (nm)	Width (μm)	Length (mm)	T_c (K)	R_N (8 K) (kΩ)	$H_{c2}(0)$ (T)	H_g (T)	T (K)	D	z	ν
S1	30	10	1	7.2	5	15.6	1.75	3	2	5	1.5
							1.5	3.5	2	4.5	1.7
							1.1	4	2	4	1.5
							0.75	4.5	2	3.7	1.8
							0.5	4.8	2	3	0.99
							0.4	5	2	3.2	1.2
							0.1	5.5	2	2	0.99
S2	15	20	1.5	7	7.23	16.25	1.35	3	2	4.9	0.99
							0.88	3.5	2	3.8	1
							0.6	4	2	4	0.9
							0.402	4.5	2	3.5	0.7
							0.1	5	2	3.5	1
							0.06	5.5	2	3	0.9
S3	15	10	1	6.9	9.35	16.02	0.88	3	2	4.5	0.9
							0.55	3.5	2	4.2	1
							0.35	4	2	4	1.5
							0.1	4.875	2	4.3	1
							0.05	5.13	2	4	1.7
B1	30/20	7.6	0.1	4.75	0.065	8.12	0.15	2.17	3	2	0.99
							0.08	2.5	3	2	0.99
							0.035	3	3	2	0.99
B2	15/4	20	1	5.45	2.65	10.6	0.87	2.2	2	4.5	1.85
							0.62	2.5	2	4.5	1.5
							0.45	3	2	4.1	1.5
							0.25	3.5	2	4	0.9
							0.1	3.9	2	3	0.9
							0.05	4.1	2	3	0.9
B3	15/4	10	1	5.05	5.06	10.76	0.4	2.1	2	6	1.5
							0.3	2.5	2	5	1.1
							0.25	3	2	5.5	1.2
							0.09	3.5	2	4	0.9

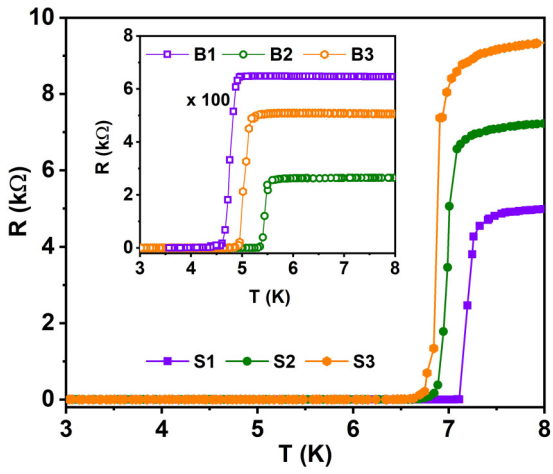


FIG. 1. Resistive transitions of NbRe films (main panel) and NbRe/Py bilayers (inset) measured at zero magnetic field. Note that the resistance of sample B1 in the inset $R(T)$ curve has been multiplied by a factor of 100 for clear representation, since it has a significantly lower normal state resistance compared to the other samples.

field of a 12 nm Py films is only 2 mT [36]). As a result, the Py magnetization remains fully saturated and aligned in-plane throughout the entire measurement range, yielding a static and homogeneous magnetic configuration.

As a representative example, Figs. 2(a) and 2(b) show the log-log scaled IVCs of sample S1 at fixed $T = 3.0$ K with varying field and fixed $H = 0.1$ T with varying temperature, respectively. The critical parameters H_g and T_g can be determined from these plots by identifying the distinct transition behavior (marked by black lines) of the I–V curves and by following the same procedure as described elsewhere [8,9]. The three distinct behaviors—negative curvature below H_g (or T_g), ohmic behavior above H_g (or T_g), and power-law near H_g (or T_g)—are clearly observed. Since the accurate determination of H_g and T_g is crucial for the VG phase analysis, in addition to the model described in Refs. [8,9], we independently verified these parameters by using the derivative method described elsewhere [5,6,37]. Following this approach, we plotted the $d(\log V)/d(\log I)$ versus current data in Figs. 2(c) and 2(d) for sample S1 at $T = 3.0$ K and $H = 0.1$ T, respectively. From these plots, the characteristic nature of the $d(\log V)/d(\log I)$ curves can be identified at low current regimes, where the

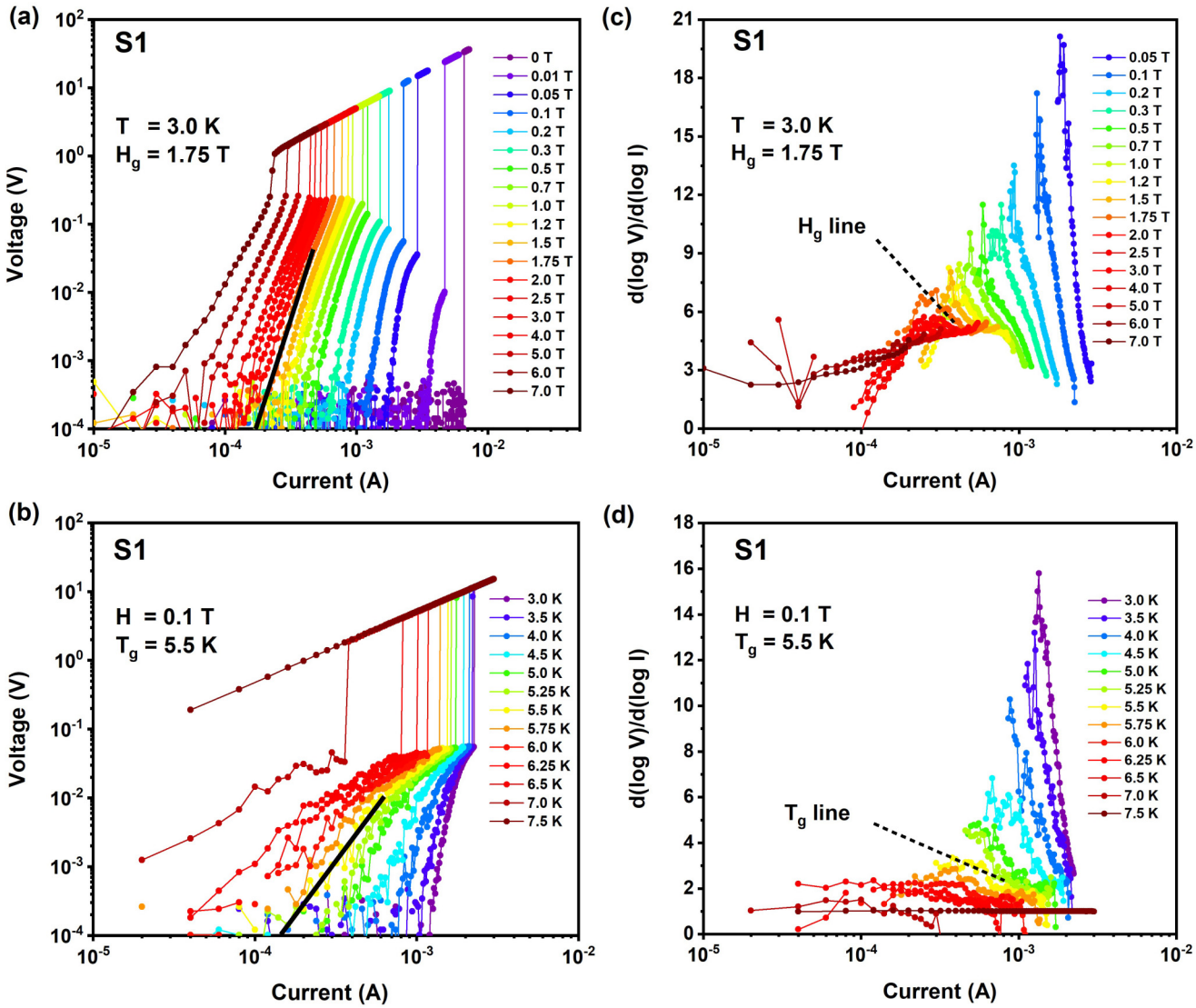


FIG. 2. Log-log scaled IVCs and their corresponding $d(\log V)/d(\log I)$ versus current plots for sample S1 at fixed temperature $T = 3.0$ K (a),(c) and fixed magnetic field $H = 0.1$ T (b),(d) as a function of magnetic field and temperature, respectively. The values of H_g and T_g are indicated in panels (a),(c) and (b),(d), respectively, and they are distinguished by the black solid and dotted lines (see more details in main text).

pronounced peak has disappeared and the curves start to show a broad downward curvature transition. This change in curvature indicates a crossover from the vortex-glass state to the vortex-liquid regime as indicated by the black dotted lines in Figs. 2(c) and 2(d), which corresponds to the H_g and T_g values. The values obtained using this method are in good agreement with those determined from Figs. 2(a) and 2(b), thereby confirming the reliability of the VG transition parameters.

Subsequently, the I–V curves can be scaled using the VG scaling laws [1,6]:

$$\frac{V}{I(H-H_g)^{\nu(z+2-D)}} = f_{\pm}\left(\frac{I}{|H-H_g|^{\nu(D-1)}}\right) \quad (1)$$

and

$$\frac{V}{I(T-T_g)^{\nu(z+2-D)}} = f_{\pm}\left(\frac{I}{|T-T_g|^{\nu(D-1)}}\right), \quad (2)$$

where ν is the critical exponent associated with the divergence of the coherence length, $\xi \sim |T-T_g|^{-\nu}$ or $\xi \sim |H-H_g|^{-\nu}$, which typically lies in the range 1–2. z is another dynamic critical exponent related to the relaxation time $\tau \sim \xi^z$, which usually lies in the range of 4–7 [1,3,4,38]. The parameter D denotes the effective dimensionality, while $f_{\pm}$ are scaling functions above and below the transition. Equations (1) and (2) are used to scale IVCs as a function of magnetic field and temperature, respectively. At $H = H_g$ and $T = T_g$, the IVC exhibits power-law behavior:

$$V(I, H_g) \propto I^{(z+1)(D-1)}, \quad V(I, T_g) \propto I^{(z+1)(D-1)}. \quad (3)$$

Simulated curves using these equations for S1 are shown as black lines in Figs. 2(a) and 2(b), for $H_g = 1.75$ T and $T_g = 5.5$ K. VG scaling was analyzed for all samples assuming quasi-2D behavior ($D = 2$) except B1 ($D = 3$), consistent with the fits shown in Figs. 3 and 4.

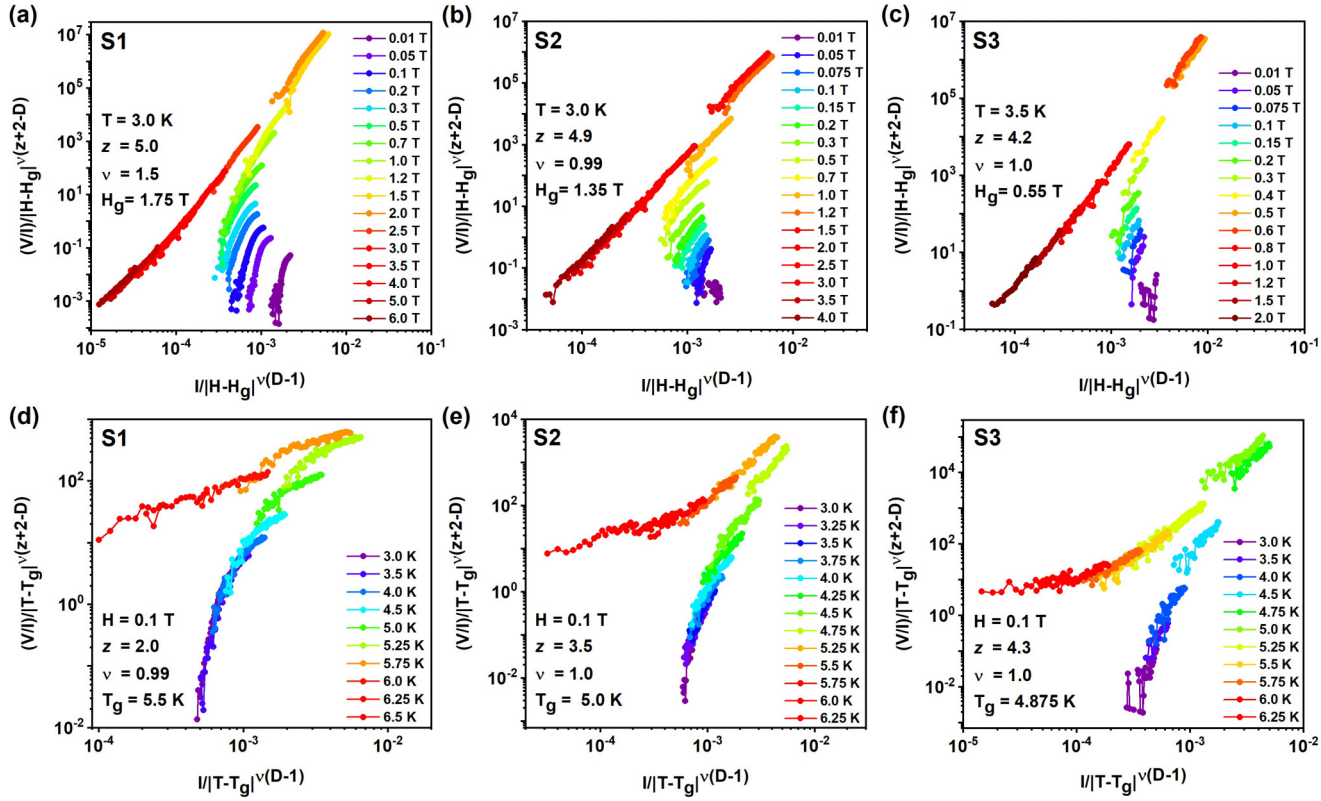


FIG. 3. IVCs in log-log scale showing VG scaling as a function of magnetic field at fixed temperatures $T = 3.0$ K (a),(b) and $T = 3.5$ K (c) for samples S1–S3. Panels (d) and (e) show IVCs in a log-log scale as a function of temperature at a fixed magnetic field $H = 0.1$ T for the same samples. The corresponding fitting parameters z, ν, H_g, and T_g are indicated for each plot.

For all IVCs, VG scaling analysis was performed using ORIGIN software based on the mathematical Eqs. (1) and (2). The procedure begins by modifying the I–V data using the transition parameters H_g and T_g according to the above scaling equations. Initial values of the critical exponents: $z = 4$–7, $\nu = 1$–2, and $D = 2$, 3 are then assigned and systematically adjusted until all I–V curves collapse onto two distinct branches. The resulting optimal values of z, ν, and H_g, which provide the best data collapse and clear separation of the I–V curves into these two branches, are summarized in Table I. In some cases, the deviations in z and ν values from the theoretical ranges may arise from vortex creep, disorder sample inhomogeneity [6], and possible dimensional crossover [8]. The VG scalings for selected temperatures as a representative case are shown in Fig. 3: panels (a) and (b) show the VG scaling for samples S1 and S2 at $T = 3.0$ K, while panel (c) shows the scaling for S3 at $T = 3.5$ K as a function of magnetic field. Panels (d)–(f) show the VG scaling of I–V at $H = 0.1$ T for samples S1, S2, and S3 as a function of temperature. Under the quasi-2D criterion ($D = 2$), the I–V isotherms collapse into two branches with reasonable fitting parameters. For $T > T_g$ and $H > H_g$, the scaled I–V isotherms exhibit excellent overlap, forming a single branch. In contrast, for $T < T_g$ and $H < H_g$, slight deviations from the scaling behavior are observed, which are likely attributable to vortex creep, which becomes increasingly significant at lower temperatures and magnetic fields. Our results indicate that the quasi-2D VG scaling model can significantly describe the behavior of NbRe films, consistent with observations in Nb [6], MgB_2 [38], FeSe [9], and TiO films [10]. Notably, deviations from ideal scaling at some fields and temperatures suggest that additional, closely spaced measurements would improve the scaling representation.

The IVCs of NbRe/Py bilayers (B1, B2, and B3) were similarly scaled through VG scaling Eqs. (1) and (2). As a representative case, the VG scaling is presented in Figs. 4(a)–4(c) for B1–B3 at a fixed temperature, $T = 3.0$ K, as a function of the magnetic field. The data collapse into two branches under $D = 2$ for B2 and B3, while B1 requires $D = 3$, indicating a dimensional crossover due to its larger thickness. Also in this case, deviations from ideal scaling at some points can be corrected by measuring additional closely spaced data points. The VG scaling below T_g or H_g presents some deviations that are most pronounced at low temperatures and low fields, where vortex creep and high current densities can obscure the scaling collapse. In contrast, at higher temperatures and magnetic fields, particularly above T_g and H_g, where thermal fluctuations become increasingly significant, the scaled data exhibit a much better collapse onto a well-defined universal curve.

The H_g values were extracted for all the samples through VG scaling on IVC and its temperature-dependent, $H_g(T)$, variation is shown in Fig. 4(d). The $H_g(T)$ trends are lower for samples of smaller dimensions compared to larger ones, except for B1. In addition, higher $H_g(T)$ values are observed for NbRe films than for NbRe/Py bilayers, as will be briefly discussed in the relevant Sec. V. This scaling analysis confirms the existence of a well-defined VG transition

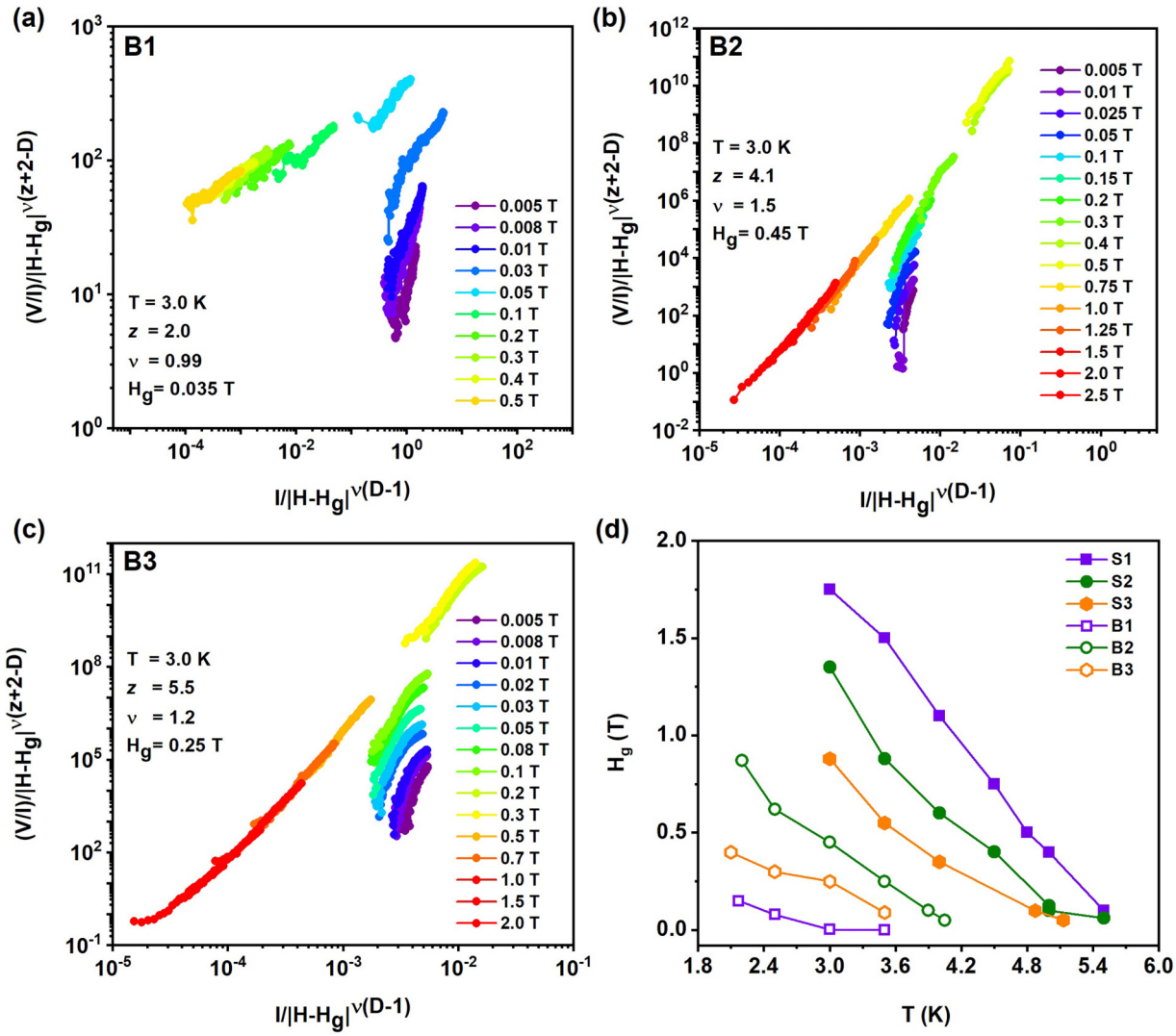


FIG. 4. IVCs in log-log scale showing VG scaling as a function of magnetic field at fixed temperature $T = 3.0$ K for NbRe/Py bilayers: (a) B1, (b) B2, and (c) B3 samples. The corresponding fitting parameters z, ν, and H_g are indicated. (d) Temperature dependence of H_g for NbRe films and NbRe/Py bilayers.

characterized by H_g and T_g. Beyond their role as scaling parameters, these quantities have a clear physical meaning: H_g marks the magnetic-field threshold at which vortices lose collective pinning and become more mobile. Therefore, the observed trends of $H_g(T)$ directly reflect the effective pinning strength and the role of dimensionality in stabilizing the VG phase. In the following sections, we build on this connection by analyzing the magnetic phase diagram and quantitatively examining vortex pinning through critical current density and pinning force measurements.

V. MAGNETIC PHASE DIAGRAM

We successfully examined the VG transition characteristics in both NbRe films and NbRe/Py bilayers. The VG scaling analysis of the IVCs reveals a clear decrease in H_g with increasing temperature as shown in Fig. 4(d), following a trend similar to that of the upper critical field, $H_{c2}(T)$. To construct a comprehensive magnetic phase diagram, we performed $R(T)$ measurements under perpendicular magnetic fields ranging from 0 to 7 T, as shown in Figs. 5(a) and 5(b) for the S2 and B2 samples, respectively. These two samples serve as representative cases, allowing a direct comparison between NbRe (15 nm) and NbRe/Py (15/4 nm) films with identical geometrical dimensions.

The $H_{c2}(T)$ values were determined at the point where resistance decreases to 50% of R_N and are plotted as red circle symbols in Figs. 5(c) and 5(d), together with the values $H_g(T)$ (wine circles) for S2 and B2, respectively. The dotted black curve in Figs. 5(c) and 5(d) represents a fit using the Ginzburg-Landau (GL) expression [39,40]:

$$H_{c2}(T) = H_{c2}(0)\frac{1-t^2}{1+t^2}, \tag{4}$$

where $t = T/T_c$ is the reduced temperature. From this fit, $H_{c2}(0)$ values for S2 and B2 are estimated to be ∼16.25 T and 10.6 T. The obtained $H_{c2}(0)$ values of other samples are mentioned in Table I.

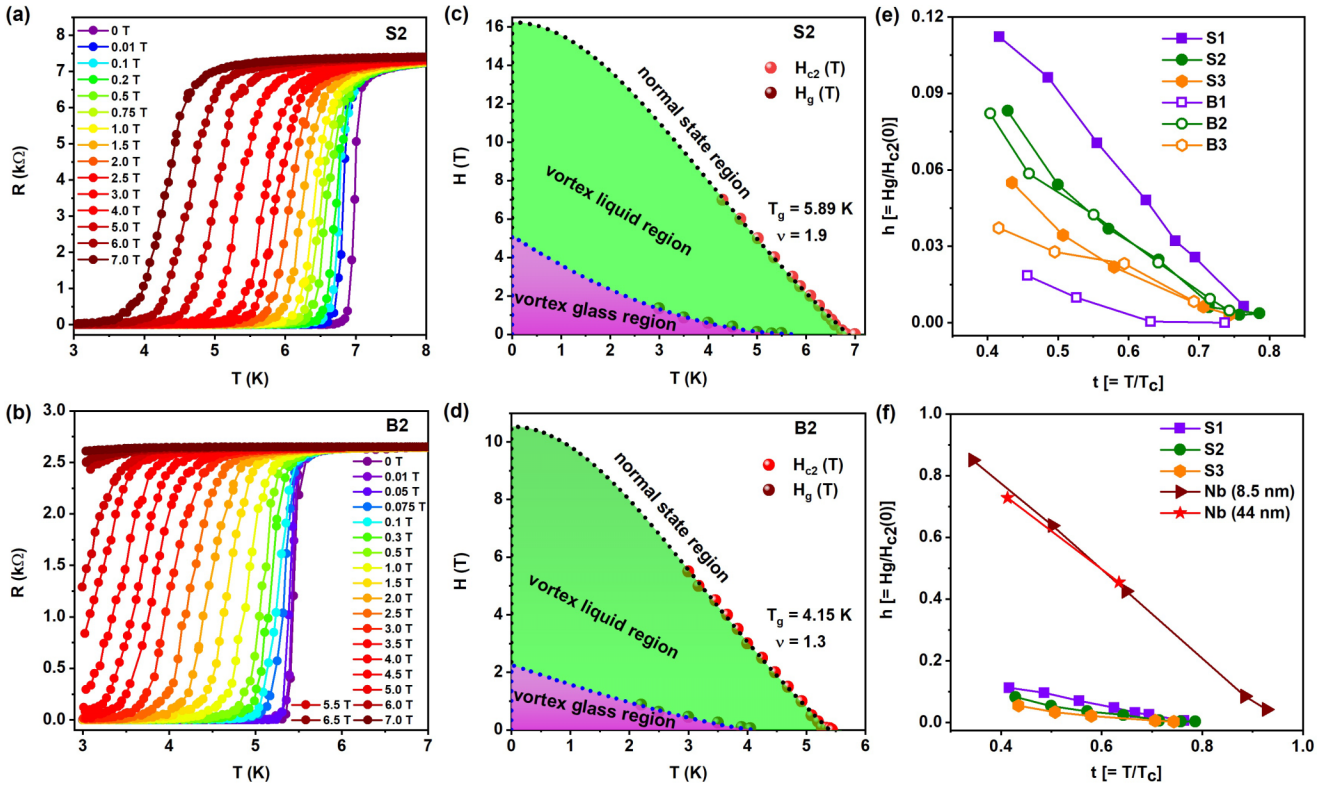


FIG. 5. (a), (b) Temperature-dependent resistance $R(T)$ for NbRe film S2 and NbRe/Py bilayer B2 under perpendicular magnetic fields from 0 to 7 T. (c), (d) $H_{c2}(T)$ and $H_g(T)$ with fitted curves and corresponding VG phase diagrams showing vortex-glass, vortex-liquid, and normal-state regions for S2 and B2, respectively (see main text for details). (e) Reduced $H_g/H_{c2}(0)$ versus $t = T/T_c$ for NbRe films, compared to Nb films [6]. (f) Reduced $H_g/H_{c2}(0)$ versus t for NbRe/Py bilayers.

The $H_g(T)$ trend was fitted using an empirical formula [18]:

$$H_g(T) \propto \left(1 - \frac{T}{T_g}\right)^{(D-1)\nu}. \tag{5}$$

The resulting fits are shown as blue dotted curves in Figs. 5(c) and 5(d) for S2 and B2, respectively, with $D = 2$ fixed and T_g and ν treated as fitting parameters. The fitted values of ν lie in the range of 1–2, which is consistent with those typically obtained from VG scaling of IVC. The VG transition temperature T_g is lower in B2 (4.15 K) than in S2 (5.89 K). From the fits of $H_{c2}(T)$ and $H_g(T)$, three distinct regions emerge: $T < T_g$ corresponds to the VG phase, $T_g < T < T_c$ defines the vortex-liquid phase, and $T > T_c$ corresponds to the normal state. These regions are illustrated in the phase diagrams of Figs. 5(c) and 5(d). The VG region in B2 seems to be suppressed relative to S2 due to the presence of the Py- ferromagnetic layer, which perturbs superconducting coherence and vortex pinning via proximity effect and pair-breaking effects [28,29,41,42]. Since the superconducting state of the samples possesses different T_c and $H_{c2}(0)$, the data presented in Fig. 4(d) was further normalized by $H_{c2}(0)$ and T_c to highlight the intrinsic evolution of the VG phase boundary and enable a more meaningful comparison. The resulting variation, $h = (H_g/H_{c2}(0))$, is plotted as a function of the reduced temperature, $t = T/T_c$, in Fig. 5(e), allowing a direct comparison between the NbRe films and NbRe/Py bilayers. The dimensionality effect can be clearly seen for $h(t)$ variation for the samples: for NbRe films, samples having larger dimension (S1) exhibit a higher $h(t)$ trend than smaller ones (S2 and S3). The same trend is also followed by NbRe/Py bilayers (B2 vs B3) but not by the sample B1. The observed lowest $h(t)$ trend in sample B1 can be ascribed to an enhanced proximity effect at the NbRe/Py interface due to the thicker Py layer, as confirmed by the lower value of T_c for this sample. H_g marks the field where a transition from VG (pinned vortices) to vortex liquid (mobile vortices) phase occurs, reflecting the combined effects of vortex pinning, thermal fluctuations, and film thickness. In larger samples, the superconducting state is more bulklike, resulting in stronger vortex pinning and a VG phase stabilized to higher fields. Smaller samples experience enhanced vortex fluctuations, weaker pinning, and more prominent edge effects, lowering $H_g(T)$. The lowest $H_g(T)$ is observed in B1 due to its reduced width and thicker Py layer, which most effectively induces a dimensional crossover and weakens flux pinning, significantly suppressing the VG phase. Collectively, the observed trends reflect the combined effects of sample size, dimensionality, and magnetic and thermal fluctuations.

Furthermore, the higher $h(t)$ trend is more pronounced in NbRe films than in NbRe/Py bilayers, likely due to the combined effect of the superconducting proximity effect and static homogeneous exchange coupling at the interface. The $h(t)$ curves for the NbRe films and their comparable NbRe/Py bilayers (e.g., S2 versus B2 and S3 versus B3) nearly overlap

at higher temperatures. This behavior can be attributed to enhanced TFs, which progressively destabilize the VG phase and reduce the relative influence of exchange-field-induced suppression, thereby diminishing the differences between the two systems. In contrast, a substantially larger separation between the $h(t)$ curves is observed for S1 versus B1 due to the stronger proximity effect induced by the thicker Py layer in B1, as discussed previously. To further clarify the proximity effect and elucidate the role of Py ferromagnet in NbRe/Py bilayers, it is worth recalling that previous works [36,43,44] have shown that Py films thinner than 125 nm exhibit homogeneous in-plane magnetization and soft hysteresis cycles with negligible coercivity. Also, since for thickness lower than 30 nm the films are expected to show Néel walls [45], the presence of the out-of-plane component of the magnetization can be excluded also at the domain walls. Consequently, since both our Py layers (4 and 20 nm thick) lie well below these thresholds, it is reasonable to interpret the suppression of the VG phase as originating from proximity and homogeneous exchange coupling instead of magnetic inhomogeneity or stray fields. Moreover, since Py has a coherence length of ∼2 nm [43], the dominant interaction is short-range exchange coupling, which modifies the quasiparticle density of states and suppresses the superconducting gap within ∼2 nm from the interface, reducing the efficiency of structural pinning centers such as grain boundaries.

We also compared the normalized H_g, $h(t)$, trends of the NbRe films (15–30 nm) with Nb films (8.5–44 nm, reported elsewhere [6]) in Fig. 5(f). The $h(t)$ trend is roughly six times smaller for NbRe than Nb films, indicating weaker effective pinning, which can be attributed to both intrinsic and microstructural effects. In fact, NbRe films consist of very small crystallites (2–3 nm) [46] compared to the larger grains in Nb. Although grain boundaries act as pinning centers, a dense network of nanoscale boundaries leads to more homogeneous and weaker collective pinning, enhancing vortex creep. As a result, vortices depin at lower magnetic fields, yielding reduced $h(t)$ behavior in NbRe compared to Nb films.

VI. CRITICAL CURRENT DENSITY AND VORTEX PINNING ANALYSIS

The reduction of the VG region, observed in the magnetic phase diagrams, particularly in NbRe/Py bilayers and in samples with reduced dimensions, indicates a weakening of vortex pinning. To clarify the origin of this behavior, we analyzed the J_c and the associated pinning mechanisms. Since J_c directly reflects the strength of vortex immobilization, its magnetic- and temperature-dependent behaviors provide a quantitative link between the VG transition parameters extracted from scaling and the underlying pinning landscape.

From the VG characteristics, it is evident that pinning strongly influences vortex dynamics. To quantify this effect, the magnetic-field-dependent $J_c(H)$ was extracted from the IVCs using a voltage criterion of 50 μV. The resulting $J_c(H)$ curves at $t \sim 0.5$ are shown in Fig. 6(a) in a linear scale (main panel) and logarithmic scale (inset) for all NbRe films and NbRe/Py bilayers. The lower $J_c(H)$ characteristics are observed in all NbRe films compared to the NbRe/Py bilayers. At zero and low magnetic fields, J_c decreases with reduced dimensions of the NbRe films, a trend mirrored in the NbRe/Py bilayers except for sample B1. The lowest J_c in B1 arises from the weakest vortex pinning due to the larger thickness of the Py layer.

The $J_c(T)$ behavior is also influenced by structural disorder and grain boundaries. Vortices interact with pinning centers via two primary mechanisms [19,23]: spatial variations in the local T_c (δT_c pinning) and fluctuations in the electronic mean free path (δl pinning) associated with structural defects. These mechanisms exhibit distinct temperature dependences, leading to characteristic forms of $J_c(t)$ in the single-vortex pinning regime (low magnetic fields) [25]. Specifically,

$$J_c^{\delta T_c}(t) = J_c(0)(1-t^2)^{7/6}(1+t^2)^{5/6} \tag{6}$$

for δT_c pinning and

$$J_c^{\delta l}(t) = J_c(0)(1-t^2)^{5/2}(1+t^2)^{-1/2} \tag{7}$$

for δl pinning.

The $J_c(t)$ curves determined at fixed $H = 0.1$ T are shown in Fig. 6(b) for the representative samples S2 (solid green color circles) and B2 (open green color circles). Fitting the data with Eqs. (6) and (7) (black and red dotted lines, respectively) shows that δT_c pinning fails to reproduce the experimental trend, while δl pinning captures the behavior with minor deviations. This indicates that δl pinning, associated with variations in the electronic mean free path due to structural disorder, dominates in these samples. A mixed pinning model combining both mechanisms

$$J_c(t) = PJ_c^{\delta T_c}(t) + (1-P)J_c^{\delta l}(t) \tag{8}$$

yields excellent fits [blue curves in Fig. 6(b)] with $P \sim 0.03$ for S2 and $P \sim 0.1$ for B2. This further confirms the predominance of δl pinning due to structural disorder, consistent with previous reports for LTS-Nb [6] and TiO films [10].

To gain additional insight into the dominant pinning mechanism, we analyzed the pinning force (F_p), defined as $F_p = J_c H$ [24]. Figure 6(c) shows $F_p(H)$ for all NbRe films and NbRe/Py bilayers at $t \sim 0.5$, which closely mirrors the $J_c(H)$ trends. All NbRe films exhibit similar F_p magnitudes, while NbRe/Py bilayers follow the same trend except B1, reflecting weaker pinning due to the thicker Py layer. These observations imply that NbRe films possess stronger pinning than NbRe/Py bilayers, which can directly influence vortex dynamics, as discussed in Sec. VII.

We further analyzed the pinning using the Dew-Hughes model [24]. Normalized pinning forces $f = F_p/F_p^{\max}$ are plotted versus reduced field $h^* = H/H_{\rm irr}$ in Fig. 6(d), where $F_p^{\max}$ is the maximum pinning force and the irreversibility field $H_{\rm irr}$ is determined as the field at which $J_c(T,H)$ extrapolates to 10^6 A/m^2 [8]. The data follow the scaling relation

$$f \propto h^{*p}(1-h^*)^q, \tag{9}$$

yielding $p \sim 0.7$, $q \sim 2.3$, and a peak position $h^*_{\max} = p/(p+q) \sim 0.23$ [black solid line in Fig. 6(d)], consistent with surfacelike pinning ($p = 1/2$, $q = 2$, and $h^*_{\max} \sim 0.2$) [8,24]. The slightly higher value of p and q may be due to inhomogeneities and disorder [47]. This confirms that structural inhomogeneities such as surface pinning are the dominant pinning centers, in agreement with observations in MgB_2 [48], NbTiN [8], TiO [10], and NbReN [47]. In NbRe/Py bilayers,

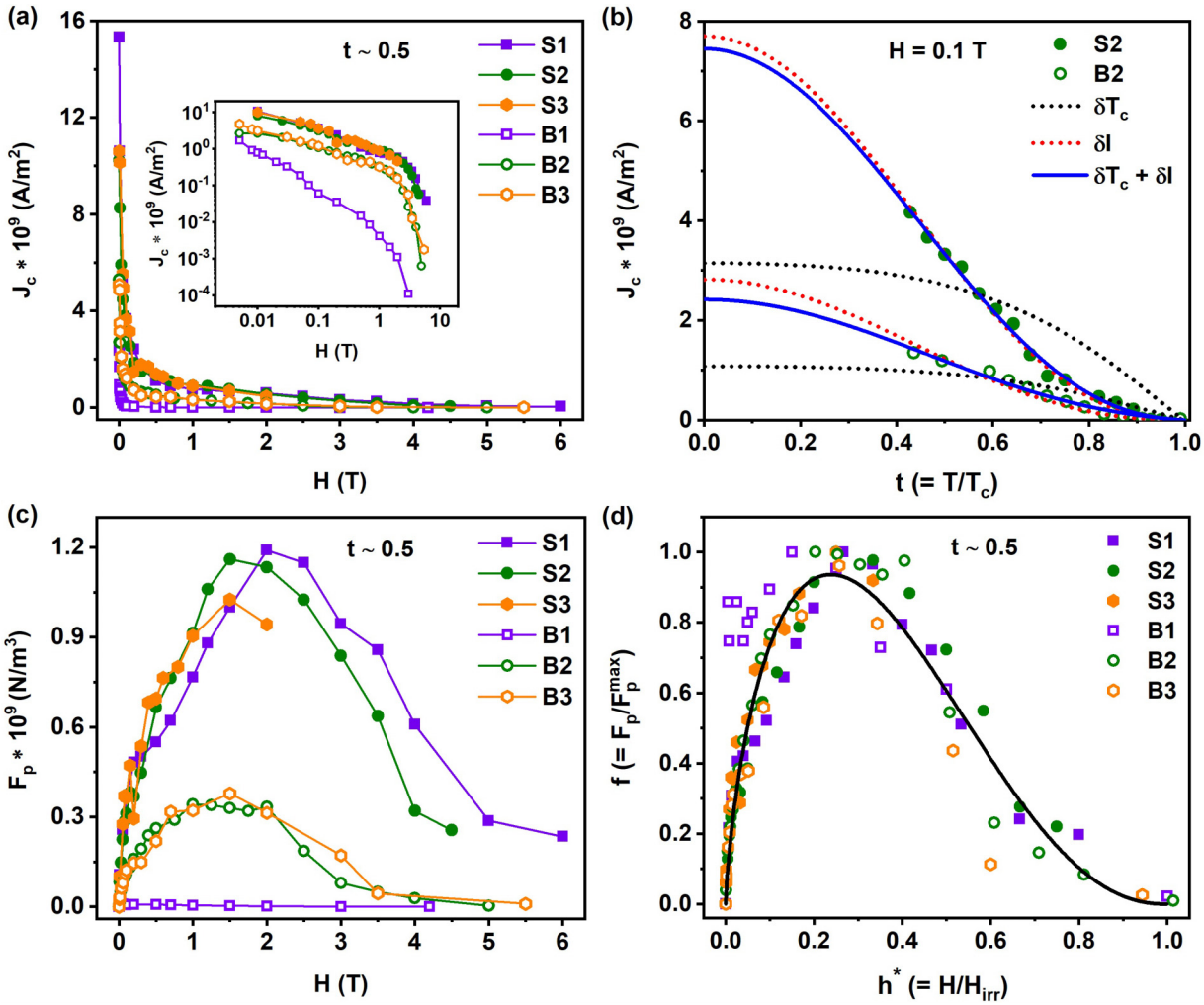


FIG. 6. (a) Magnetic field dependent critical current densities, $J_c(H)$, variation for all NbRe films and NbRe/Py bilayers at fixed reduced temperature $t = 0.5$ in a linear scale (main panel) and logarithmic scale (inset). (b) $J_c(t)$ variation for samples S2 and B2 at fixed $H = 0.1$ T, analyzed within the framework of δl, δT_c, and combined $\delta l + \delta T_c$ pinning contributions (see main text for details). (c) Pinning force, $F_p(H)$, variation for all samples at $t = 0.5$. (d) Normalized pinning force, $f = F_p/F_p^{\max}$, as a function of reduced field $h^* = H/H_{\rm irr}$, fitted with the scaling Eq. (9) (black solid curve) for both NbRe films and NbRe/Py bilayers.

the superconductor/ferromagnet interface may further modify the pinning landscape through interfacial disorder or proximity effects, contributing to the observed reduction of $H_g(T)$ and pinning strength.

VII. VORTEX INSTABILITIES AND VORTEX VELOCITIES

The strength of vortex pinning not only governs the extent of the VG phase but also significantly influences vortex dynamics in the flux-flow regime. In particular, weaker pinning facilitates enhanced vortex mobility, leading to higher v^* values. Having established the differences in pinning strength between NbRe films and NbRe/Py bilayers through the analyses of J_c and pinning forces, we now investigate vortex instabilities and the corresponding v^*, which provide a direct dynamical consequence of the VG transition behavior and pinning characteristics discussed above. Within the framework of vortex dynamics in the flux-flow state (FFS), as described by the Larkin-Ovchinnikov (LO) theory, the point before sudden jump to the normal state observed in the IVCs is identified as the vortex instability point (I^*, V^*) [28,47,49,50]. As a reference, we presented zoomed IVCs for the S1 sample only in Fig. 7(a) at $t \sim 0.5$, in which the vortex instability point is clearly visible prior to the transition from superconducting to normal state. The corresponding v^* values can be estimated using Eq. (10):

$$v^* = \frac{V^*}{\mu_0 H L}. \tag{10}$$

The extracted v^* values for NbRe films and NbRe/Py bilayers are plotted as a function of the magnetic field in Fig. 7(b) for fixed $t \sim 0.5$. For sample B1, the v^* value is approximately 2.5 times larger than that of S1 in the low-field region and remains about twice as large at higher magnetic fields. These results clearly demonstrate that v^* is systematically larger in NbRe/Py bilayers than in pure NbRe films, consistent with previous reports [28,29]. Similar enhancements in v^* have been widely reported in Nb- and NbRe-based superconducting systems upon the introduction of a ferromagnetic layer, which modifies vortex dynamics through both

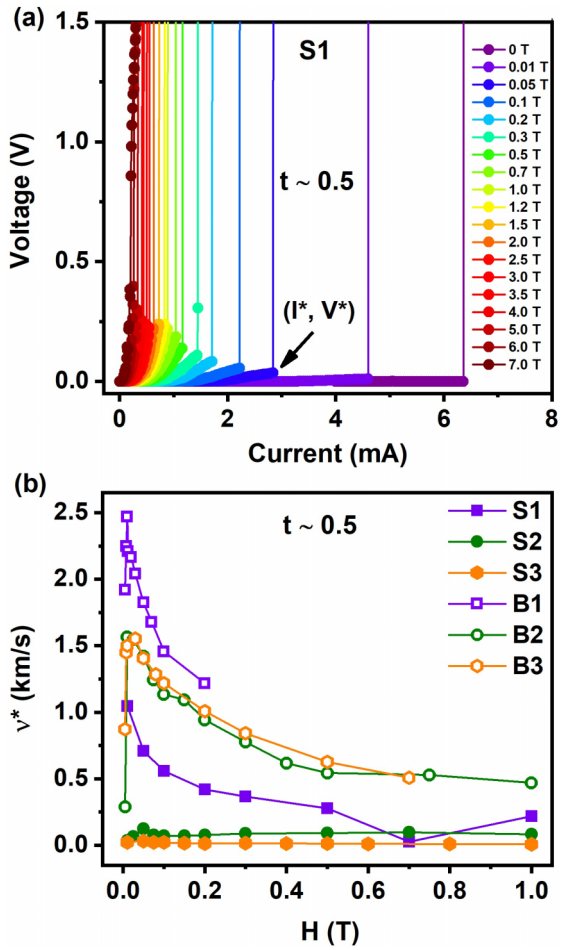


FIG. 7. (a) Zoomed view of IVC for the S1 sample at $t \sim 0.5$ marked with the vortex instability point (I^*, V^*). (b) Vortex velocity (v^*) variation as a function of magnetic field for NbRe films and NbRe/Py bilayers at fixed reduced temperature $t = 0.5$.

increased quasiparticle scattering processes and a strong depression of the order parameter at the interface due to the exchange energy E_{ex} present in F [28,29,41,42]. Although the enlarged vortex core expected in S/F hybrids [51] would reduce the LO critical velocity, the experimentally observed enhancement of v^* can be attributed to efficient quasiparticle escape and enhanced energy relaxation at the S/F interface, which dominate the nonequilibrium vortex dynamics.

In addition to these considerations, the effective pinning strength in NbRe/Py bilayers is clearly weaker than in NbRe films, as discussed in Secs. IV–VI. This reduced pinning strength promotes faster vortex motion and thus further enhances v^*, an effect that must be considered when analyzing vortex dynamics in such hybrid structures. Moreover, v^* increases with increasing film thickness: thicker NbRe films (S1) exhibit higher v^* than thinner ones (S3) and a similar trend is observed for NbRe/Py bilayers, where B1 shows higher v^* than B3. Overall, v^* is lower in NbRe films than in NbRe/Py bilayers because the ferromagnetic Py layer significantly alters vortex dynamics in the superconducting NbRe layer. In pure NbRe films, vortex motion is constrained by stronger intrinsic pinning arising from structural defects, leading to higher vortex viscosity and reduced velocities. In contrast, in NbRe/Py bilayers, superconducting proximity effect and homogeneous magnetic exchange interaction modify the pinning landscape, effectively reducing the pinning force, as illustrated in Fig. 6(c). These magnetic interactions further assist vortex motion through exchange-field-mediated coupling between vortices and the ferromagnetic Py layer.

This interpretation is also supported by Figs. 5(e) and 5(d), where the VG region is more extended for NbRe films than the NbRe/Py bilayers. Below H_g, vortices remain strongly pinned, whereas above H_g they depin and enter a liquidlike state. Accordingly, the higher H_g in NbRe films leads to lower v^*, while the reduced H_g in NbRe/Py bilayers results in higher v^*. For both NbRe films and NbRe/Py bilayers, H_g decreases with decreasing sample thickness and a corresponding reduction in v^* is observed. This behavior can be attributed to dimensionality effects: in thinner films, the effective vortex volume is reduced and enhanced disorder and surface roughness strengthen pinning, thereby suppressing vortex mobility.

Recently, we also investigated FFS in NbRe/Au (S/N) and NbRe/Py (S/F) bilayers, where gold (Au) is a normal metal (N) [29]. Although proximity-induced modifications of the superconducting state are observed in both systems, the ferromagnetic Py layer produces substantially stronger effects than the nonmagnetic Au layer. In particular, the v^* reaches approximately 1.6 km/s in the S/F bilayer, compared with about 0.7 km/s in the S/N counterpart, while the quasiparticle relaxation time is reduced from ~150 ps in NbRe/Au to ~24 ps in NbRe/Py. These results indicate that ferromagnetism plays a decisive role in determining the vortex dynamics through the combined action of superconducting proximity effects and exchange-field-induced pair breaking. Consequently, the enhanced vortex response observed in NbRe/Py bilayers cannot be attributed solely to a generic proximity effect, but rather to the presence of the ferromagnetic layer itself. Motivated by these findings, our broader objective is to optimize NbRe-based S/F heterostructures for SSPDs, where ultrafast quasiparticle relaxation and high v^* are desirable for achieving improved device performance, as demonstrated in previous studies [28,29].

VIII. CONCLUSIONS

In summary, we fabricated superconducting NbRe films and NbRe/Py bilayers of comparable widths and thicknesses on Si substrates using dc magnetron sputtering. These samples were systematically investigated through IVC as a function of magnetic field and temperature, revealing clear signatures of a VG phase transition. The VG behavior was analyzed using VG scaling theory, with particular emphasis on extracting the characteristic parameters T_g and H_g. On this basis, comparative magnetic phase diagrams were constructed for NbRe films and NbRe/Py bilayers of similar dimensions, identifying three distinct regimes: vortex glass, vortex liquid, and the normal state.

A systematic downward shift of the $H_g(T)$ line was observed in NbRe/Py bilayers compared to NbRe films due to superconducting proximity effect and homogeneous magnetic exchange coupling at the NbRe/Py interface, with a further

reduction upon decreasing the sample dimensions. This behavior is consistent with weaker vortex pinning in the bilayers and aligns with trends reported in other layered or disordered superconductors. The reduced $H_g(T)$ values directly indicate weaker pinning in NbRe/Py bilayers, a conclusion corroborated by the analysis of critical current densities and pinning forces, which are consistently lower than in NbRe films. The pinning properties in both systems are strongly influenced by structural inhomogeneities and disorder.

Consistent with these findings, the evaluated critical vortex velocities are higher in NbRe/Py bilayers than in NbRe films, reflecting their reduced pinning strength and enhanced vortex mobility. Overall, our results indicate that NbRe/Py bilayers, owing to their faster vortex dynamics, may be promising candidates for superconducting device applications requiring rapid vortex response, such as SSPDs and other superconducting electronic devices. Nevertheless, further studies involving systematic control of interface properties and ferromagnetic layer thickness will be necessary to fully disentangle the roles of dimensionality, disorder, and proximity effects in governing the VG phase and vortex dynamics.

ACKNOWLEDGMENT

We acknowledge Professor S. Pagano's group for providing access to the wire bonding facility used to make the electrical contacts.

DATA AVAILABILITY

There are no publicly available research data or software supporting this manuscript. Requests for further information or data should be sent to the authors.

[1] R. H. Koch, V. Foglietti, W. J. Gallagher, G. Koren, A. Gupta, and M. P. A. Fisher, Experimental evidence for vortex-glass superconductivity in Y-Ba-Cu-O, Phys. Rev. Lett. **63**, 1511 (1989).

[2] H. Yamasaki, K. Endo, S. Kosaka, M. Umeda, S. Yoshida, and K. Kajimura, Quasi-two-dimensional vortex-glass transition observed in epitaxial $Bi_2Sr_2Ca_2Cu_3O_x$ thin films, Phys. Rev. B **50**, 12959 (1994).

[3] Y. Z. Zhang, R. Deltour, J. F. de Marneffe, H. H. Wen, Y. L. Qin, C. Dong, L. Li, and Z. X. Zhao, Vortex characteristics in a superconducting $Bi_2Sr_{2-x}La_xCuO_{6+\delta}$ thin film, Phys. Rev. B **62**, 11373 (2000).

[4] M. C. Sullivan, R. A. Isaacs, M. F. Salvaggio, J. Sousa, C. G. Stathis, and J. B. Olson, Scaling analysis of the static and dynamic critical exponents in underdoped, overdoped, and optimally doped $Pr_{2-x}Ce_xCuO_{4-y}$ films, Phys. Rev. B **81**, 134502 (2010).

[5] J. E. Villegas and J. L. Vicent, Vortex-glass transitions in low-T_c superconducting Nb thin films and Nb/Cu superlattices, Phys. Rev. B **71**, 144522 (2005).

[6] S. M. Altanany, I. Zajcewa, T. Zajarniuk, A. Szewczyk, and M. Z. Cieplak, Vortex dynamics in disordered niobium thin films, Phys. Rev. B **109**, 214504 (2024).

[7] S. K. Gupta, S. Sen, A. Singh, D. K. Aswal, J. V. Yakhmi, E.-M. Choi, H.-J. Kim, K. H. P. Kim, S. Choi, H.-S. Lee, W. N. Kang, and S.-I. Lee, $I-V$ characteristic measurements to study the nature of the vortex state and dissipation in MgB_2 thin films, Phys. Rev. B **66**, 104525 (2002).

[8] Z.-Y. Han, T.-Y. Jing, J. Yang, W.-B. Cai, and Z.-Q. Li, Vortex-glass transition and vortex pinning behavior in three-dimensional NbTiN epitaxial films, Supercond. Sci. Technol. **37**, 055011 (2024).

[9] W.-L. Zhao, X. Zhu, Z.-H. He, K.-H. Gao, and Z.-Q. Li, The vortex state in FeSe superconducting thin film, Supercond. Sci. Technol. **33**, 105010 (2020).

[10] C. Zhang, F. Hao, X. Liu, Y. Fan, T. Wang, Y. Yin, and X. Li, Quasi-two-dimensional vortex–glass transition and the critical current density in TiO epitaxial thin films, Supercond. Sci. Technol. **31**, 015016 (2018).

[11] A. W. Tsen, B. Hunt, Y. D. Kim, Z. J. Yuan, S. Jia, R. J. Cava, J. Hone, P. Kim, C. R. Dean, and A. N. Pasupathy, Nature of the quantum metal in a two-dimensional crystalline superconductor, Nat. Phys. **12**, 208 (2016).

[12] S. Dutta, J. Jesudasan, and P. Raychaudhuri, Magnetic field induced transition from a vortex liquid to Bose metal in ultrathin a-MoGe thin film, Phys. Rev. B **105**, L140503 (2022).

[13] C. Huang, E. Zhang, Y. Zhang, J. Zhang, F. Xiu, H. Liu, X. Xie, L. Ai, Y. Yang, M. Zhao, J. Qi, L. Li, S. Liu, Z. Li, R. Zhan, Y.-Q. Bie, X. Kou, S. Deng, and X. Xie, Observation of thickness-tuned universality class in superconducting β-W thin films, Sci. Bull. **66**, 1830 (2021).

[14] E. Zhang, J. Zhi, Y.-C. Zou, Z. Ye, L. Ai, J. Shi, C. Huang, S. Liu, Z. Lin, X. Zheng, N. Kang, H. Xu, W. Wang, L. He, J. Zou, J. Liu, Z. Mao, and F. Xiu, Signature of quantum Griffiths singularity state in a layered quasi-one-dimensional superconductor, Nat. Commun. **9**, 4656 (2018).

[15] A. Kumar, S. Husale, M. P. Saravanan, B. Gajar, M. Yousuf, A. Saini, M. G. Yadav, and R. P. Aloysius, Current–voltage characteristics of focused ion beam fabricated superconducting tungsten meanders, Nanotechnology **35**, 015705 (2024).

[16] R. P. Aloysius, S. Husale, A. Kumar, F. Ahmad, A. K. Gangwar, G. S. Papanai, and A. Gupta, Superconducting properties of tungsten nanowires fabricated using focussed ion beam technique, Nanotechnology **30**, 405001 (2019).

[17] A. Abrikosov, The magnetic properties of superconducting alloys, J. Phys. Chem. Solids **2**, 199 (1957).

[18] D. S. Fisher, M. P. A. Fisher, and D. A. Huse, Thermal fluctuations, quenched disorder, phase transitions, and transport in type-II superconductors, Phys. Rev. B **43**, 130 (1991).

[19] G. Blatter, M. V. Feigel'man, V. B. Geshkenbein, A. I. Larkin, and V. M. Vinokur, Vortices in high-temperature superconductors, Rev. Mod. Phys. **66**, 1125 (1994).

[20] S. Eley, A. Glatz, and R. Willa, Challenges and transformative opportunities in superconductor vortex physics, J. Appl. Phys. **130**, 050901 (2021).

[21] F. Laviano, R. Gerbaldo, G. Ghigo, L. Gozzelino, G. P. Mikitik, T. Taen, and T. Tamegai, Evidence of anisotropic vortex pinning by intrinsic and irradiation-induced defects in $Ba(Fe, Co)_2As_2$ studied by quantitative magneto-optical imaging, Supercond. Sci. Technol. **27**, 044014 (2014).

[22] M. Feigel'man, V. Geshkenbein, and A. Larkin, Pinning and creep in layered superconductors, Physica C **167**, 177 (1990).

[23] R. Griessen, H.-h. Wen, A. J. J. van Dalen, B. Dam, J. Rector, H. G. Schnack, S. Libbrecht, E. Osquiguil, and Y. Bruynseraede, Evidence for mean free path fluctuation induced pinning in $YBa_2Cu_3O_7$ and $YBa_2Cu_4O_8$ films, Phys. Rev. Lett. **72**, 1910 (1994).

[24] D. Dew-Hughes, Flux pinning mechanisms in type II superconductors, Philos. Mag. **30**, 293 (1974).

[25] R. Prozorov, N. Ni, M. A. Tanatar, V. G. Kogan, R. T. Gordon, C. Martin, E. C. Blomberg, P. Prommapan, J. Q. Yan, S. L. Bud'ko, and P. C. Canfield, Vortex phase diagram of $Ba(Fe_{0.93}Co_{0.07})_2As_2$ single crystals, Phys. Rev. B **78**, 224506 (2008).

[26] B. J. Ruck, J. C. Abele, H. J. Trodahl, S. A. Brown, and P. Lynam, Vortex dynamics and instabilities in layered and homogeneous Ta/Ge superconductors, Phys. Rev. Lett. **78**, 3378 (1997).

[27] C. Cirillo, G. Carapella, M. Salvato, R. Arpaia, M. Caputo, and C. Attanasio, Superconducting properties of noncentrosymmetric $Nb_{0.18}Re_{0.82}$ thin films probed by transport and tunneling experiments, Phys. Rev. B **94**, 104512 (2016).

[28] M. Caputo, C. Cirillo, and C. Attanasio, NbRe as candidate material for fast single photon detection, Appl. Phys. Lett. **111**, 192601 (2017).

[29] F. De Chiara, Z. M. Kakhaki, F. Avitabile, F. Colangelo, A. Kumar, C. Attanasio, and C. Cirillo, Fast vortex dynamics and relaxation times in NbRe-based heterostructures, Beilstein J. Nanotechnol. **17**, 292 (2026).

[30] M. Ejrnaes, C. Cirillo, D. Salvoni, F. Chianese, C. Bruscino, P. Ercolano, A. Cassinese, C. Attanasio, G. P. Pepe, and L. Parlato, Single photon detection in NbRe superconducting microstrips, Appl. Phys. Lett. **121**, 262601 (2022).

[31] C. Cirillo, M. Ejrnaes, P. Ercolano, C. Bruscino, A. Cassinese, D. Salvoni, C. Attanasio, G. P. Pepe, and L. Parlato, Single photon detection up to 2 μm in a pair of parallel microstrips based on NbRe ultrathin films, Sci. Rep. **14**, 20345 (2024).

[32] C. Cirillo, J. Chang, M. Caputo, J. W. N. Los, S. Dorenbos, I. E. Zadeh, and C. Attanasio, Superconducting nanowire single photon detectors based on disordered NbRe films, Appl. Phys. Lett. **117**, 172602 (2020).

[33] F. Avitabile, F. Colangelo, M. Y. Mikhailov, Z. M. Kakhaki, A. Kumar, I. E. Zadeh, C. Attanasio, and C. Cirillo, Superconducting nanowire single photon detectors based on NbRe nitride ultrathin films, Appl. Phys. Lett. **127**, 172601 (2025).

[34] C. Cirillo, M. Rovirola, C. González, B. Casals, J. M. Hernàndez, F. Macià, A. García-Santiago, and C. Attanasio, Spin pumping in NbRe/Co superconductor-ferromagnet heterostructures, Supercond. Sci. Technol. **36**, 074001 (2023).

[35] F. Colangelo, M. Modestino, F. Avitabile, A. Galluzzi, Z. M. Kakhaki, A. Kumar, J. Linder, M. Polichetti, C. Attanasio, and C. Cirillo, Unveiling intrinsic triplet superconductivity in noncentrosymmetric NbRe through inverse spin-valve effects, Phys. Rev. Lett. **135**, 226002 (2025).

[36] S. Voltan, C. Cirillo, H. J. Snijders, K. Lahabi, A. García-Santiago, J. M. Hernández, C. Attanasio, and J. Aarts, Emergence of the stripe-domain phase in patterned permalloy films, Phys. Rev. B **94**, 094406 (2016).

[37] D. R. Strachan, M. C. Sullivan, P. Fournier, S. P. Pai, T. Venkatesan, and C. J. Lobb, Do superconductors have zero resistance in a magnetic field? Phys. Rev. Lett. **87**, 067007 (2001).

[38] H. Yang, Y. Jia, L. Shan, Y. Zhang, H.-H. Wen, C. Zhuang, Z. Liu, Q. Li, Y. Cui, and X. Xi, I–V characteristics of the vortex state in MgB_2 thin films, Phys. Rev. B **76**, 134513 (2007).

[39] M. Tinkham, *Introduction to Superconductivity*, 2nd ed. (McGraw-Hill, New York, 2004).

[40] A. Kumar, F. Colangelo, F. Avitabile, Z. Makhdoumi Kakhaki, C. Cirillo, and C. Attanasio, Electron energy relaxation times in superconducting tungsten rhenium-based thin films, Supercond. Sci. Technol. **39**, 025017 (2026).

[41] C. Attanasio and C. Cirillo, Quasiparticle relaxation mechanisms in superconductor/ferromagnet bilayers, J. Phys.: Condens. Matter **24**, 083201 (2012).

[42] C. Cirillo, V. Pagliarulo, H. Myoren, C. Bonavolontà, L. Parlato, G. P. Pepe, and C. Attanasio, Quasiparticle energy relaxation times in NbN/CuNi nanostripes from critical velocity measurements, Phys. Rev. B **84**, 054536 (2011).

[43] C. Cirillo, A. García-Santiago, J. M. Hernandez, C. Attanasio, and J. Tejada, Magnetic properties of double exchange biased diluted magnetic alloy/ferromagnet/antiferromagnet trilayers, J. Phys.: Condens. Matter **25**, 176001 (2013).

[44] C. Cirillo, S. Voltan, E. A. Ilyina, J. M. Hernández, A. García-Santiago, J. Aarts, and C. Attanasio, Long-range proximity effect in Nb-based heterostructures induced by a magnetically inhomogeneous permalloy layer, New J. Phys. **19**, 023037 (2017).

[45] T. Trunk, M. Redjdal, A. Kákay, M. F. Ruane, and F. B. Humphrey, Domain wall structure in permalloy films with decreasing thickness at the Bloch to Néel transition, J. Appl. Phys. **89**, 7606 (2001).

[46] C. Cirillo, M. Caputo, G. Divitini, J. W. A. Robinson, and C. Attanasio, Polycrystalline NbRe superconducting films deposited by direct current magnetron sputtering, Thin Solid Films **758**, 139450 (2022).

[47] C. Cirillo, V. Granata, A. Spuri, A. Di Bernardo, and C. Attanasio, NbReN: A disordered superconductor in thin film form for potential application as superconducting nanowire single photon detector, Phys. Rev. Mater. **5**, 085004 (2021).

[48] D. C. Larbalestier, L. D. Cooley, M. O. Rikel, A. A. Polyanskii, J. Jiang, S. Patnaik, X. Y. Cai, D. M. Feldmann, A. Gurevich, A. A. Squitieri, M. T. Naus, C. B. Eom, E. E. Hellstrom, R. J. Cava, K. A. Regan, N. Rogado, M. A. Hayward, T. He, J. S. Slusky, P. Khalifah, *et al.*, Strongly linked current flow in polycrystalline forms of the superconductor MgB_2, Nature (London) **410**, 186 (2001).

[49] A. I. Larkin and Y. N. Ovchinnikov, Nonlinear conductivity of superconductors in the mixed state, Sov. Phys. JETP **41**, 960 (1975).

[50] Z. M. Kakhaki, A. Leo, A. Spuri, M. Ejrnaes, L. Parlato, G.P. Pepe, F. Avitabile, A. Di Bernardo, A. Nigro, C. Attanasio, and C. Cirillo, Characterization of quasiparticle relaxation times in

microstrips of NbReN for perspective applications for superconducting single-photon detectors, Mater. Sci. Eng., B **304**, 117376 (2024).

[51] S. L. Prischepa, M. Y. Kupriyanov, C. Cirillo, and C. Attanasio, Magnetic memory effect in type-II superconductor/ferromagnet bilayers, Supercond. Sci. Technol. **27**, 055024 (2014).